^{2}H(p,2p)n at 508 MeV: Recoil momenta $\leq$200 MeV/c

V. Punjabi,[a] K. A. Aniol,[b] A. Bracco,[c]* C. A. Davis,[c]† M. B. Epstein,[b]
H. P. Gubler,[c]‡ J. P. Huber,[b] W. P. Lee,[c]§ D. J. Margaziotis,[b] C. F. Perdrisat,[a]
P. R. Poffenberger,[c]** H. Postma,[d] H. J. Sebel,[d]††
A. W. Stetz,[e] and W. T. H. van Oers[c]†

[a]*College of William and Mary, Williamsburg, Virginia 23185*
[b]*California State University, Los Angeles, California 90032*
[c]*University of Manitoba, Winnipeg, Manitoba, Canada R3T 2N2*
[d]*University of Technology, Delft, The Netherlands*
[e]*Oregon State University, Corvallis, Oregon 97331*

(Received 16 August 1988)

Differential cross sections for the reaction ^{2}H(p,2p)n at T_p=507 and 508 MeV are presented. The kinematics selected included two quasi-free angle pairs: 41.5°-41.4° and 30.1°-53.75°; in addition, data away from the quasi-free condition were obtained in four symmetric angle pairs: 38.1°-38.0°, 44.1°-44.0°, 47.1°-47.0°, and 50.0°-50.0°, and five asymmetric angles pairs: 30.1°-37.0°, 30.1°-44.0°, 30.1°-61.0°, 30.1°-68.0°, and 41.5°-50.0°. The data range over an energy window 100 MeV wide on one of the proton energies, the second energy being defined by the kinematic condition of a single neutron recoiling. The data are compared with the impulse approximation prediction and with the results of a nonrelativistic calculation of the six lowest-order Feynman diagrams describing the reaction. A previously known missing strength for the reaction in the small neutron recoil region is confirmed with much smaller experimental uncertainty; the missing strength persists up to 150 MeV/c neutron recoil. The onset of a systematic cross section excess relative to the impulse approximation near neutron recoil momentum 200 MeV/c is explored in detail.

I. INTRODUCTION

The single-nucleon knockout reaction $A(p,2p)A-1$ on a nucleus A has been studied intensively starting in the mid 1960s. During the same period the impulse approximation (IA) was proposed by Serber[1] and Chew and Wick,[2] which is the basis for an understanding of the reaction in the quasielastic mode and was subjected to numerous tests. Review articles summarizing this early phase were published by Jacob and Maris,[3] Riou,[4] Jackson and Berggren[5] and others. The most recent review article for the reaction is the one by Kitching *et al.*[6]

In the IA description of a (p,2p) knockout reaction, the incident proton interacts elastically via the strong interaction with a single proton, while the remaining nucleons in the target nucleus are merely spectators. Thus in the first-order interaction diagram, as illustrated Fig. 1(a) for the deuteron, the spectator momentum $\mathbf{p}_5$ is equal to the negative of the internal momentum $\mathbf{q}$ of the struck proton, $\mathbf{p}_5=-\mathbf{q}$. As a consequence the cross section can be factorized into the following expression:

$$d^3\sigma/d\Omega_3 dT_3 d\Omega_4 = K(d\sigma/d\Omega)^{pp}_{\text{c.m.}} |\Phi(\mathbf{p}_5)|^2 , \quad (1)$$

where 3 and 4 are the scattered and ejected protons and 5 is the neutron spectator as in Fig. 1(b). The quantity K is a kinematic factor given in Sec. IV, $(d\sigma/d\Omega)^{pp}_{\text{c.m.}}$ is the half-off-energy-shell elastic pp differential cross section and $|\Phi(\mathbf{p}_5)|^2$ is the single-nucleon momentum density.

The simple IA picture needs to be corrected for effects such as multiple scattering, final-state interactions (FSI), meson exchange currents (MEC), and isobar configurations (IC). An additional difficulty, which is encountered in the analysis of any single-nucleon knockout experiment, is the inherent off-shell nature of nucleons bound in a nuclear environment. Was the ejected nucleon the only one to be off-shell (as assumed by Gross[7]), or are all nucleons in a nucleus off-shell (as is the case in the Blankenbecler-Sugar[8] view)?

The strong interaction of a hadronic probe with nucleons other then the ejected proton and of the two hadrons in the final state generally leads to a rapid depletion of the strength of the quasielastic channel as the mass of the target nucleus increases, or with increasing binding of the ejected nucleon. With the advent of electron accelerators with improved duty cycles at Saclay, Bates (MIT), and NIKHEF (Amsterdam), the (e,$e'p$) reaction has become an important source of information on shell-model state occupation probabilities, and internal momentum distributions derived from (p,2p) data have been looked at with some suspicion.

The situation is quite different for light nuclei. In this case FSI and multiple-scattering effects are small and can be calculated; the study of the reaction offers an interesting testing ground for various theoretical models. One definite advantage of the protonic probe over the electromagnetic one is that at intermediate energies the NN differential cross section is only weakly dependent upon the collision energy or momentum transfer, whereas for the electromagnetic probe it is notoriously sensitive to both. It has also become clear that the quasielastic reaction $A(e,e'p)A-1$, even on the lightest nuclei, is not free of distortions. Ultimately the same nuclear structure information must come from both reactions. Compara-

tive studies of the hadron- and electron-induced reactions might thus be necessary before a better understanding of both reactions mechanisms is finally achieved.

Although several experiments in the early 1970s at Space Radiation Effects Laboratory (SREL) (Refs 9 and 10) and Clinton P. Anderson Meson Physics Facility[11] (LAMPF) have revealed intriguing features for the $^2H(p,2p)n$ reaction, these features were never fully explained. There was an apparent lack of strength of the reaction at small neutron momenta when compared with the IA prediction, and also a spectacular deviation from the IA starting at 200 MeV/c recoil in several kinematics of the final state.

Among the unanswered questions raised by previous studies of the reaction, the occupation number is of central importance. For the deuteron it is synonymous with the number of nucleons participating in the reaction. Typically, previous $^2H(e,e'p)n$ and $^2H(p,2p)n$ experiments have determined the nucleon number in the deuteron with combined statistical and systematic uncertainties no better than 10–20 %.

The Saclay[12] data for the $^2H(e,e'p)n$ reaction and their recent extension to very large neutron recoil momenta by the Bonn group,[13] are well known. Arenhoevel[14] has shown that it is indispensable to include MEC, FSI, as well as the Δ part of IC to reproduce these results on the basis of one of the standard NN potential deutron wave functions like the Paris[15] or Reid soft core[16] (RSC) potentials. Yet, closer examination of this apparent agreement reveals surprisingly large discrepancies between data and theoretical calculations, up to 25%, even at very small neutron recoil momentum. These differences might be due in part to large systematic uncertainties in the data, or they may indicate a more fundamental problem.

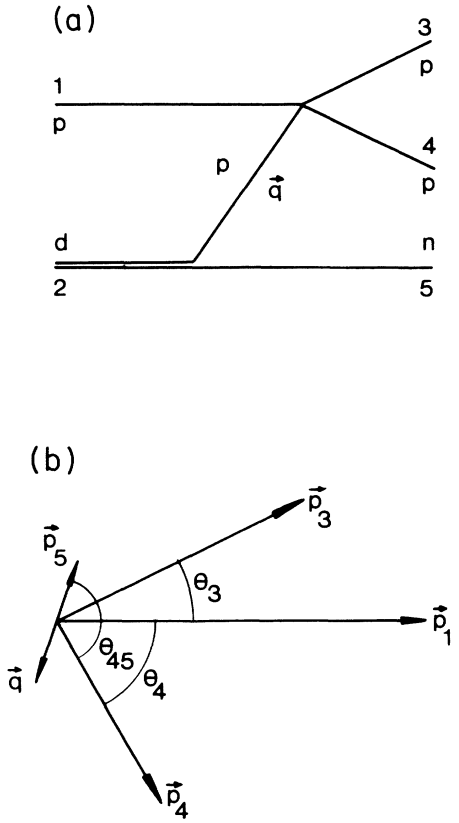

FIG. 1. (a) The Feynman diagram for quasielastic pp scattering. (b) Kinematical diagram showing the labeling of the reaction participants: $1+2\rightarrow 3+4+(5)$, where (5) is the unobserved neutron.

The considerations above were at the origin of the reinvestigation of the $^2H(p,2p)n$ reaction which will be reported in the present paper and its sequel, which will hereafter be referred to as part II. The expectation was that an extensive and consistent data base for $^2H(p,2p)n$ over a large sector of the final-state phase space, would bring new insights, and possibly help elevate these data to the same level of confidence as $(e,e'p)$ data.

The present paper will be referred to as part I, and will include data for neutron recoil momenta up to 200 MeV/c, a kinematical range well below the region where Δ excitation is important, yet one where deviations from the IA are already visible. The data $q>200$ MeV/c will appear subsequently in part II. The present paper will be organized as follows. In Sec. II the various components of the experiment are described, including beam, target, and detection system. In Sec. III details of the data analysis will be given, with particular attention to the determination of the target thickness. A discussion of the impulse approximation, which is central to the analysis of all single-nucleon knockout reactions, is in Sec. IV; also described is a calculation of the $(p,2p)$ cross section including the two IA graphs for pp and pn scattering, and, in addition, two double scattering and two FSI graphs. The results of this calculation will be referred to in the remainder of the present paper as the "complete calculation." The experimental results are presented and discussed in Sec. V. The conclusion is in Sec. VI.

II. EXPERIMENTAL METHOD

The experiment was performed at the TRIUMF cyclotron laboratory in Vancouver, Canada, over a period of two years in 1983 and 1984. In the first part (EX83) the proton beam energy was 507±1 MeV and in the second part (EX84) it was 508±1 MeV. In both phases of the experiment the energy spread of the beam was typically 1 MeV full width at half maximum (FWHM). The beam position and spot size at the target were monitored by viewing a fluorescent ZnS screen placed temporarily at the target position. The beam divergence and spot size at the target were found to be approximately ±0.2 mrad and 0.25 cm^2, respectively. The beam intensity was monitored by a secondary electron-emission monitor (SEM) located downstream from the target and also by a Faraday cup for part of the experiment. Beam currents used in this experiment were between 0.1 to 10 nA.

A. The liquid D_2 target

The liquid deuterium target was built for this experiment at the Delft University of Technology (see Ref. 17) to fit inside a vessel which originally contained a liquid helium-4 target.[18] Figure 2 shows the cryostat and the

two identical target cells. The target cells could be raised, lowered, and rotated remotely. The internal diameter of the cells was 55 mm, and their frame was 6 mm thick, with windows made from a 0.025-mm-thick stainless-steel foil. With this design of the frame it was possible to make measurements with up to 150° between the two outgoing protons. The cells were operated at a pressure of 250±2 mb, resulting in some bulging of the foils. The determination of the target thickness is discussed in Sec. III B.

B. Detection system

A schematic diagram of the detection system is shown in Fig. 3. Two protons were detected in coincidence by the magnetic spectrometer (MRS) positioned on the left-hand side (lhs) relative to the beam and counter telescopes positioned on the right-hand side (rhs). In EX83 one counter telescope was used, in EX84 six were used, as seen in Fig. 3.

The MRS spectrometer[19] contains two optical elements, a horizontally focusing quadrupole and a dipole. Particles are bent vertically, and focusing onto the bend plane is provided by the shaping of the dipole entrance and exit magnetic field edges. Three multiwire proportional chambers (MWPC) for EX83, and three sets of drift chambers for EX84, provided position information for particle trajectory tracking. The trigger of the MRS was derived from a coincidence of fast signals from plastic scintillator detectors at the entrance of the spectrometer and above the dipole in the focal-plane area.

In EX83 a thin plastic scintillator ΔE_b (0.079 cm thick) located in front of the lower MWPC, provided a timing signal which was part of the MRS trigger requirement. The MWPC located in front of the quadrupole at a distance of 163.0 cm from the target allowed definition of the solid angle with software cuts. Two MWPC's mounted on either side of the focal plane, followed by a 2.5-cm-thick plastic scintillator completed the detection system. The wire spacing in all three MWPC's was 0.2 cm.

In EX84 three sets of drift chambers were used. The front end chamber set (FEC) consisted of a vertical and horizontal wire plane and was located in front of the quadrupole. Each plane had two sets of wires which were separated by 0.5 cm. The drift direction was within the plane of the chamber. The two other drift chambers were placed in the vicinity of the focal plane, and were of the "vertical" drift, or "MIT"-type[20] (VDC); in these, the drift direction was perpendicular to the chamber plane. These chambers were oriented nearly parallel to the focal plane, and at ≈45° to the particle trajectories, ensuring charge collection on typically three to five wires for a good event.

Two plastic scintillator counters ΔE_{b0} and ΔE_{b1} were located in front of the FEC at distances of 145.8±0.1 cm and 135.0±0.1 cm from the target, respectively. The ΔE_{b0} detector had a 1.7±0.005 cm diameter hole carved in a 8.0×8.0 cm^2 plastic scintillator. The ΔE_{b1} detector was 3.5±0.005 cm in diameter; both were 0.154 cm thick. Either one could be used to define the LHS solid angle. There were ten plastic scintillators above the top drift chamber, completely covering the focal plane. In both experiments the time-of-flight (TOF) path through the spectrometer was approximately 11 m. The angular

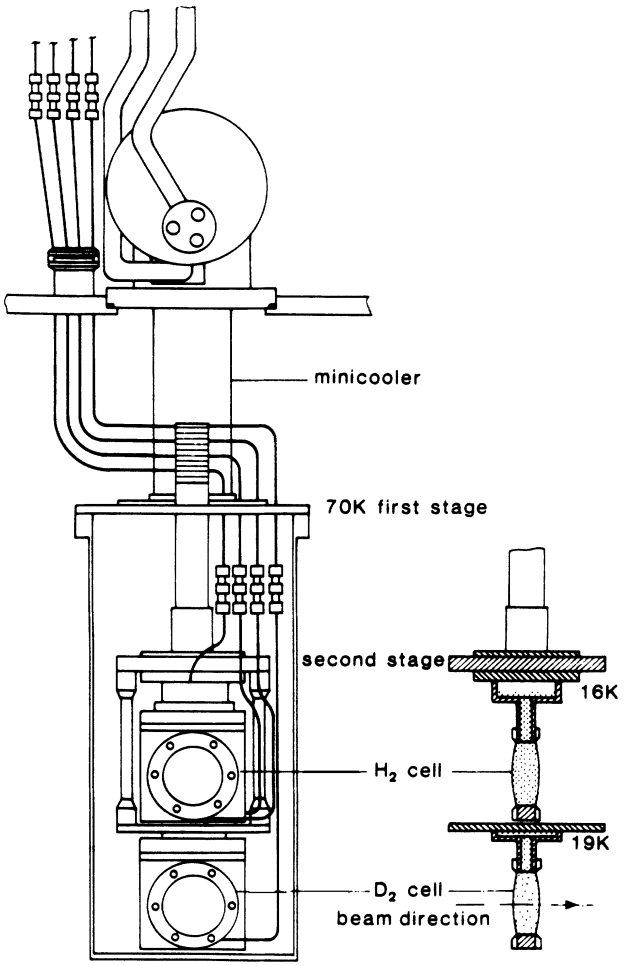

FIG. 2. Liquid hydrogen and deuterium cryostat, showing the geometry of the two target cells.

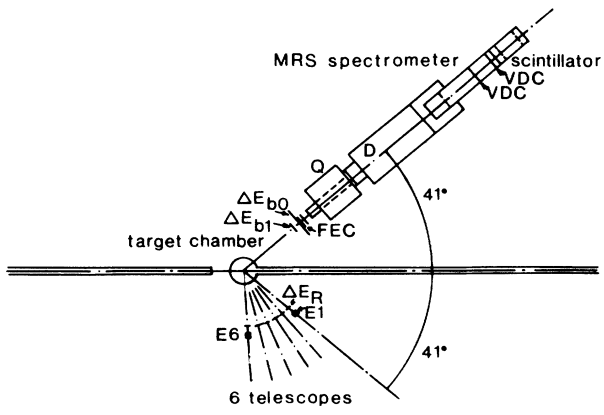

FIG. 3. Experimental setup showing the magnetic spectrometer MRS on the left-hand side of the beam, and the six scintillation telescopes on the right-hand side.

position of the MRS was known and reproducible to $\pm 0.02°$.

The rhs proton counter telescope in EX83 consisted of a plastic scintillator 6.35 cm in diameter and 0.32 cm thick which defined the solid angle on that side, and of a NaI (Tl) crystal, 12.7 cm in diameter and 15.2 cm thick. This crystal was able to stop 233.0 MeV protons. A Cu absorber was placed between the plastic and the NaI (Tl) detectors when the proton energy was larger than the range limit in the crystal. The distance from the scattering center to the plastic scintillator was 195.7 cm. In EX84 six counter telescopes were used, numbered $E1$ to $E6$ as shown in Fig. 3. Each consisted of a plastic scintillator detector ΔE_R, used to define the solid angle, and a NaI (Tl) detector. For telescope $E1$ the plastic scintillator was 8.0 cm in diameter and 0.32 cm thick. The remaining five telescopes had 6.35-cm-diam plastic scintillators of the same thickness. Counter telescopes $E1$ to $E4$ used NaI (Tl) crystals 15.2 cm thick and 12.7 cm in diameter, the remaining two crystals were of the same diameter but only 7.6 cm thick. The distance from the scattering center to each plastic scintillator counter was 200.0 cm, except for $E1$, for which it was 205.7 cm. As in EX83, a Cu absorber was used, when necessary, to stop the protons in the NaI (Tl). The telescopes were mounted on a platform and positioned with an accuracy of $\pm 0.05°$.

The momentum calibration of the MRS was obtained by taking advantage of the two-body kinematics of elastic pp scattering from hydrogen. Single-proton events in the MRS were recorded for a fixed magnetic field in the MRS and several values of the MRS angle to select proton energies covering the energy range of interest. The energy calibration of the counter telescopes was obtained by measuring proton-proton events from hydrogen at a series of different angle pairs covering the relevant range of energies.

In both experiments a coincidence trigger was formed requiring signals from the ΔE scintillation counters on the lhs and rhs and from the focal-plane-area scintillators in the MRS; the NaI (Tl) detectors were not part of the trigger. In analyzing the EX84 data corresponding to approximately zero neutron recoil momentum and equal angles of the proton (41.5°-41.4°), no requirement was imposed on the amount of energy deposited in the NaI (Tl) crystals, thus adding no software condition to the hardware trigger for the rhs particle. For the rest of the data a software energy window was placed on T_4, based on the NaI (Tl) signal. This procedure would reject pions which can be produced in kinematics with large neutron recoils, and also would reject low-energy protons coming from the second kinematical solution which occurs for part of the data. For these data an efficiency correction was applied to correct for the fraction of protons stopping short of their range because of nuclear interactions in Cu or NaI. The efficiency values of Bracco *et al.*[21] were used.

III. DATA ANALYSIS AND CROSS SECTIONS

The data were stored on magnetic tape and analyzed event-by-event on a mainframe computer at the College of William and Mary. The analysis program prepared all the histograms necessary, with cuts on the left-to-right TOF, on the dE/dx information from the scintillators, and on the solid angle on the MRS side if required. A correction for the energy loss in the absorbers was calculated and correction factors for the MWPC (EX83) or drift chamber (EX84) inefficiencies were obtained for the kinematics at which data were taken. A factor to correct for dead time in the experiment was obtained, and when appropriate, a correction was applied for event losses due to inelastic reactions in the Cu absorber and NaI (Tl) crystal in the rhs detectors. Momenta $\mathbf{p}_3$ and $\mathbf{p}_4$ were calculated for the two protons in the events selected. The missing momentum is defined as $\mathbf{p}_5=\mathbf{p}_1-(\mathbf{p}_3+\mathbf{p}_4)$; in the absence of any other particle, such as a pion, $\mathbf{p}_5$ is then the momentum of the recoiling neutron. Selected events were binned and displayed in a two-dimensional plot (T_4 versus T_3), showing the energy locus corresponding to quasielastic events. Finally the differential cross sections and statistical uncertainties were calculated for a number of T_3 bins, each of fixed width ΔT_3 corresponding to a small range of the neutron recoil momentum $\mathbf{p}_5$.

A. Initial analysis

The events used to calculate the differential cross sections were subjected to a number of tests concerning the wire pattern in the MWPC or drift chambers. For EX83 an event was rejected if any of the MWPC chambers showed no wire hits, or if more than five wires had been hit in any chamber. Events with two to five wires in the hit pattern were kept provided any gap in the pattern was no more than two wires wide. With the drift chambers in EX84, events with no hits or more than two wires hit in the FEC planes were rejected; for the VDC planes only events with three, four, and five adjacent wires hit were accepted. Accidental coincidence events were subtracted using a sample of events selected in exactly the same way as coincident events, but with their origin in two different beam bursts. The live-time factor was determined from the ratio of pulses received by the computer versus those sent simultaneously to light-emitting diodes (LED) attached to each plastic scintillator and NaI (Tl) crystal; the rate at which the LED's were fired was proportional to the beam intensity, determined by an accidental coincidence between the beam monitor and a constant frequency pulse generator.

B. *pp* differential cross section and target thickness

The event rate for pp elastic scattering was compared with published values of the pp differential cross section to determine the target thickness both in EX83 and in EX84.

The number of pp events per incident proton was measured with the same experimental setup and beam energy as for $^2H(p,2p)$, the deuterium being replaced by hydrogen in the same target cell. Both in EX83 and in EX84 the primary measurement was made at the proton angles 41.6°-41.6°, corresponding to 90° in the c.m. The two final-state proton energies were very nearly the same as

for the corresponding ^{2}H($p,2p$) data point. The target areal density was then calculated from the known solid angle, applying efficiency and dead-time corrections. The best available *pp* differential cross-section data were used for a scattering angle of 90° in the c.m. at 500 (Ref. 22) and 515 MeV,[23] which gave an interpolated value of 3.44±0.06 mb/sr (c.m.) at 508 MeV; this value is 1.1% smaller than the phase-shift analysis prediction of Arndt *et al.*[24] The liquid hydrogen thickness was then obtained using tabulated density values at the pressure of the experiment, 250 mbar, which corresponds to a temperature of 16.9 K. The target thickness was found to be 0.753±0.015 cm in EX83 and 0.887±0.018 cm for EX84. A mechanical measurement in EX84 at 37 K and at the same pressure of 250 mbar with the use of micrometers gave 0.917±0.005 cm. An independent measurement at the High Flux Reactor in Petten (The Netherlands), using 24 keV neutrons and published *np* cross sections gave 0.880±0.012 cm, in agreement with the result of the *pp* differential cross-section measurement. The increase in thickness from EX83 to EX84 was due to accidental overpressurization of the cell having caused permanent deformation of the foils.

A secondary *pp* differential cross-section measurement uses the target thickness given above, at an angle of 66° c.m. The result, 3.87±0.05 mb/sr (c.m.), is in agreement with the unpublished[25] value 3.829±0.087 mb/sr at 497.5 MeV and 66.36° (c.m.); it is 6.0% larger than the prediction of the phase-shift analysis of Ref. 24.

The number of deuterium atoms in the cell was then calculated from the 90° *pp* result using tabulated ratios of molar densities for liquid hydrogen and deuterium. The results for the areal density were $n=(3.88\pm0.08)\times10^{22}$ D/cm^2 for EX83 and $n=(4.56\pm0.09)\times10^{22}$ D/cm^2 for EX84. The data were taken after sufficient time for the liquids to be in thermal equilibrium. By analyzing the reproducibility of 17 identical ^{2}H($p,2p$) runs at 41.5°-41.4° it is estimated that fluctuations of the target density under the condition and for the duration of the experiment were less than ±0.25%.

C. ^{2}H($p,2p$) differential cross sections

The fivefold differential cross section is obtained from

$$d^3\sigma/d\Omega_3 d\Omega_4 dT_3 = N/(\Delta\Omega_3\Delta\Omega_4\Delta T_3 nI\epsilon_1\epsilon_2\epsilon_3)\ , \quad (2)$$

where N is the number of events within an energy interval ΔT_3 and within solid angle intervals $\Delta\Omega_3$ on the MRS side, and $\Delta\Omega_4$ on the telescope side. The number of deuterons per unit of area in the target is n, and the number of incident protons as determined from the monitor count is I. The quantity ϵ_1 is an efficiency correction factor for the MWPC's (EX83) or drift chamber (EX84); ϵ_2 is the live-time factor correcting for the electronics and computer dead time and ϵ_3 is a factor correcting for the fraction of protons removed from the full range peak by inelastic processes in the Cu absorber (when used) and NaI (Tl) crystal in the RHS telescope when the T_4 information was used.

A very narrow peak in a histogram of T_3 appeared in the EX84 data at the angle pair 41.5°-41.4° at a sum energy (T_3+T_4) equal to the beam energy; this peak corresponds precisely to elastic scattering on hydrogen, and provides an additional check of the energy calibration; it is an indication of a hydrogen contamination in the deuterium. A detailed analysis of this region of the data, with a software cut on solid angle to reduce the width of the peak by taking advantage of the two-body nature of the reaction, gave a value of 1.5×10^{-3} for the fraction of hydrogen to deuterium atoms.

D. Resolution correction

In exclusive ($p,2p$) experiments the cross section is a function of the final-state kinematic variables $\mathbf{p}_3$ and $\mathbf{p}_4$. However, the variables of interest according to the IA are the recoil momentum $\mathbf{p}_5$ and the excitation energy $E_{\rm exc}=M_x-m_{A-1}$, where M_x is the missing mass defined by $M_x^2=(p_1+p_2-p_3-p_4)^2$, m_{A-1} is the mass of the residual target in its ground state, and the p_i's are four momenta. For the deuteron the residual target mass is the mass of the neutron, and $E_{\rm exc}=0$. The only variable of interest is then $\mathbf{p}_5=-\mathbf{q}$, and five kinematical quantities ($\mathbf{p}_3$, θ_4, and ϕ_4) are measured. We will present experimental results as fivefold differential cross sections as a function of the kinetic energy T_3, and also as a momentum space density $|\Phi(\mathbf{p}_5)|^2$ (calculated from the differential cross sections as explained in 1.1), versus the neutron recoil momentum p_5.

The value of p_5 calculated using energy and momentum conservation was corrected using a Monte Carlo (MC) simulation which included the finite acceptance of

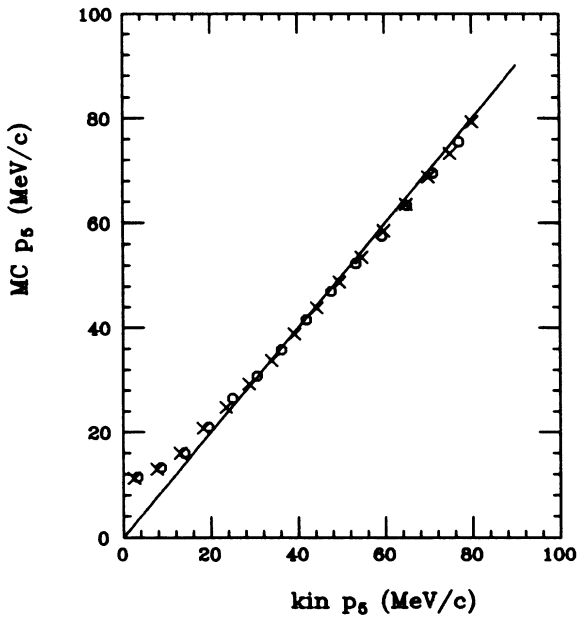

FIG. 4. Result of the Monte Carlo simulation showing the most likely neutron recoil momentum p_5 (MC) vs the central value of p_5 (kin p_5) calculated from the detector central angles and momentum. The proton angles are 41.5°-41.4°; the symbols (○) and (×) correspond to the proton kinetic energy $T_3<T_{30}$ and $T_3>T_{30}$, respectively, where T_{30} is for $p_5=0$.

the detectors. MC events were generated by choosing the five independent variables $(p_3,\theta_3,\phi_3,\theta_4,\phi_4)$ of the experiment uniformly over the intervals defined by the experimental geometry, and assuming the three nucleon masses. Each event was weighted according to the theoretical probability for the neutron recoil of the event. For each energy interval, ΔT_3, one observes a distribution of p_5 values due to the finite solid angles, as well as target thickness and beam size. Furthermore, multiple scattering in the target and assorted foils is included. The most likely value of p_5 is then determined. Calling the most likely value p_5 (MC), the results of the MC simulation for 41.5°-41.4° are shown as a function of the kinematical values of p_5 (kin p_5) in Fig. 4. The correction is largest near zero recoil, and for this particular choice of proton angles changes sign at $p_5 \approx 40$ MeV/c. When angles and momenta are chosen so as to place $p_5=0$ in the center of the acceptance, the finite-size acceptance in these quantities allows events with $p_5 \neq 0$. The most likely p_5 value becomes larger than zero because the acceptance for events with $p_5=0$ is smaller than that for $p_5 \neq 0$. For other values of $p_5 \neq 0$, the probability for events with $p_5 < p_5$ (central) becomes much larger than that for $p_5 > p_5$ (central), and the most likely value of p_5 is smaller than p_5 (central).

IV. IMPULSE APPROXIMATION AND NEXT-ORDER CORRECTIONS

A. Prescriptions of the impulse approximation

First each one of the three terms in the IA cross section (1) given in Sec. I will be specified. In the case of $^2H(p,2p)n$, neglecting the proton-neutron mass difference, the kinematic factor K has the following form:

$$K=\frac{s_{34}p_3p_4^2}{p_1\,|\,E_5p_4-E_4p_5\cos\theta_{45}\,|}\ ,$$

where all quantities are defined in the laboratory frame, and the notation follows the kinematical diagram of Fig. 1 (b). The angle θ_{45} is between $\mathbf{p}_4$ and $\mathbf{p}_5$ and $s_{34}=(p_3+p_4)^2$, where p_3 and p_4 are four momenta.

The momentum density $|\Phi(\mathbf{p}_5)|^2$ represents the probability of finding the proton with internal momentum $-\mathbf{q}=\mathbf{p}_5$; it is normalized as follows:

$$4\pi\int|\Phi(\mathbf{p}_5)|^2q^2dq=n_p\ ,$$

where n_P is the apparent probability of finding a proton in the deuteron.

Finally the half-off-energy-shell pp differential cross section in (1) will be replaced here by the free pp differential cross section evaluated at the laboratory collision energy T_{pp} defined by s_{34}, and at the c.m. scattering angle δ_{pp} defined by the invariant (p_1-p_3), as follows:

$$T_{pp}=(s_{34}-4m_p^2)/2m_p\ ,$$

and with

$$(p_1-p_3)^2_{\text{c.m.}}=(p_1-p_3)^2_{\text{lab}}\ ,$$

then

$$\cos\delta_{pp}=(E_1^*E_3^*+p_1p_3\cos\theta_3-E_1E_3)/p_1^*p_3^*\ ,$$

where the quantities with an asterisk are defined in the pp c.m.

B. Double scattering and final-state interaction

In an attempt to gain as much information about the elementary reaction mechanism involved in the $^2H(p,2p)n$ reaction as possible, calculations have been made of the differential cross section following the Feynman diagram approach and including IA pp and pn scattering (IA_{pp} and IA_{pn}) as well as double scattering of the projectile and FSI among the two nucleons of the deuteron, following the work of Glauber[26] and Wallace.[27] The six corresponding diagrams and the notation used here are shown in Fig. 5; some results of this calculation were presented earlier.[28] The calculation uses nonrelativistic NN amplitudes and a noncovariant deuteron wave function; however, all kinematic variables are calculated relativistically. Spin is fully taken into account and the Paris NN potential deuteron wave function[29] is used; the NN amplitudes are evaluated on-shell from the helicity amplitudes of Arndt *et al.*[24] obtained from phase-shift analysis. Cross sections were also calculated with the Moscow[30] potential deuteron wave function for the high precision 41.5°-41.4° kinematics.

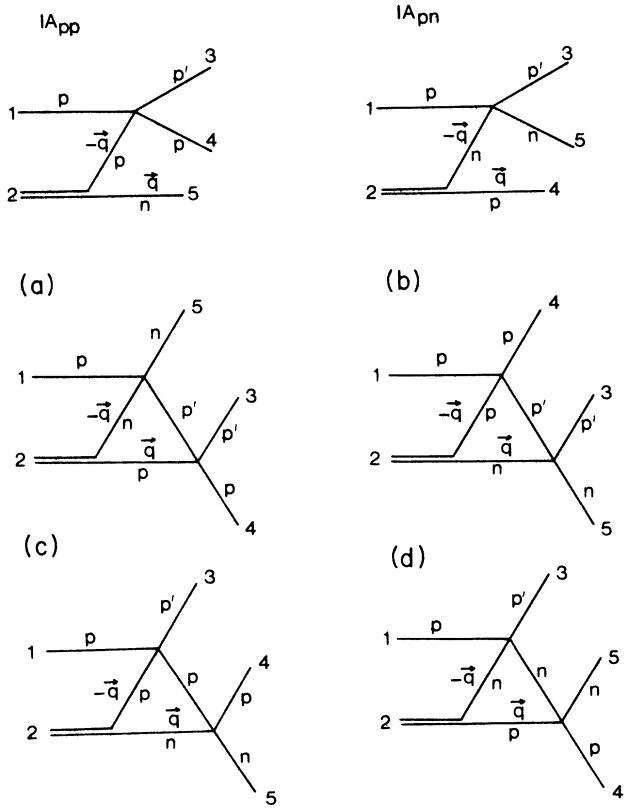

FIG. 5. The six lowest-order Feynman graphs for $^2H(p,2p)n$. IA_{pp} is the dominant graph at small neutron momenta; (a) and (b) are rescattering graphs, and (c) and (d) are FSI graphs.

C. Multiple-scattering formulas

The multiple-scattering series is expressed in terms of the scattering matrix τ, which is the solution of the three-body Lippman-Schwinger equation. Keeping only energy conserving terms up to double scattering, τ can be written as

$$\begin{aligned}\tau=&\tau_{p'p}+\tau_{p'n}-i\pi\tau_{p'p}\delta(E-H_0)\tau_{p'n}\\&-i\pi\tau_{p'n}\delta(E-H_0)\tau_{p'p}-i\pi\tau_{pn}\delta(E-H_0)\tau_{p'p}\\&-i\pi\tau_{pn}\delta(E-H_0)\tau_{p'n}\ ,\end{aligned}\tag{3}$$

where the indices of the τ matrix are p' for the projectile in the final state, p, and n for the deuteron constituents. The total energy is E and H_0 is the free-particle Hamiltonian. The first two terms are for IA pp and pn scattering, respectively, as in Fig. 5. In the following they will be labeled IA_{pp} and IA_{pn}. The third and fourth terms, graphs (a) and (b) of Fig. 5, include one rescattering step for the projectile with the neutron (a), or with the proton (b), respectively. The last two terms include FSI among the two nucleon constituents of the deuteron, after interaction of the projectile with the proton (c), or with the neutron (d), respectively, as shown in graphs (c) and (d) of Fig. 5. The relation between the τ matrix of (3) and the usual T matrix is

$$\langle f|\tau|i\rangle=-(2\pi)^3\delta^3(\mathbf{p}_f-\mathbf{p}_i)\prod_{\text{initial}}\frac{1}{\sqrt{2VE_i}}\times\prod_{\text{final}}\frac{1}{\sqrt{2VE_f}}\langle f|T|i\rangle\ ,\tag{4}$$

where $\mathbf{p}_{i,f}$ and $E_{i,f}$ are the total momentum and energy in the initial and final states, respectively. The one-particle states are normalized in a box of volume V. In terms of the T matrix the fivefold differential cross section has the usual form

$$\begin{aligned}&d^3\sigma/d\Omega_{p'}d\Omega_p dT_{p'}\\&\quad=\frac{p_3p_4^2}{(2\pi)^5 32m_d p_1|E_5p_4-p_5E_4\cos\theta_{45}|}\\&\qquad\times\tfrac{1}{6}\sum_{LMS}|\langle\mathbf{p}_3\mathbf{p}_4\mathbf{p}_5,L|T|0,M;\mathbf{p}_1,S\rangle_A|^2\ ,\end{aligned}\tag{5}$$

where the factor of $\frac{1}{6}$ arises from averaging over the initial spin states, and labels 3 and 4 refer to the two protons, 5 to the neutron. The sum is over the eight orthogonal final three-nucleon spin states $|L\rangle$, the three z components of the deuteron spin M, and the two spin states of the projectile S; A indicates antisymmetrization. The dynamics of the interaction are contained in the three body T matrix in (5). These half-off-shell T-matrix elements can be expressed in terms of the on-shell, two-nucleon amplitudes M_{ss} and $M_{mm'}$ $(m,m'=-1,0,+1)$ of Stapp *et al.*,[31] which are then calculated using the phase-shift analysis results of Ref. 24.

After antisymmetrization of the two-proton part of the final-state wave function, each term in (3) contributes 48 amplitudes. For the IA_{pp} term,

$$T_{LMS}=4(2\pi)^{5/2}\sqrt{2m_d}\times\sum_{m=-1}^{+1}[A_{LMS}(\theta,\phi)\mp A_{LMS}(\pi-\theta,\pi+\phi)]\Phi_M^m(\mathbf{q})\ .\tag{6}$$

For the pp rescattering term in (1),

$$T^a_{LMS}=i2(2\pi)^{2/3}\sqrt{2m_d}\int_{\mathbf{p}_{34}}d^2q\sum_{m=-1}^{+1}[B^a_{LmS}(\theta,\phi,\theta',\phi')\mp B^a_{LmS}(\pi-\theta,\pi+\phi,\theta',\phi')]\times\Phi_M^m(\mathbf{q})\sqrt{s}\sqrt{s'}/|P_{34}E_q-qE_{34}\cos\theta_q|\ ,\tag{7}$$

where the summation is over m, the z projection of the total nucleon spin in the deuteron, and for graph (a) in Fig. 5 $\mathbf{q}$ is the internal momentum of the proton at the deuteron vertex. The angles $\theta,\phi(\theta',\phi')$ are c.m. scattering angles and the factors $\sqrt{s}$ $(\sqrt{s'})$ are the two-nucleon invariant energies at the first and second vertex, respectively. In the denominator of Eq. (7), $P_{34}=|\mathbf{p}_3+\mathbf{p}_4|$ and $E_{34}=E_3+E_4$, and θ_q is the angle between $\mathbf{q}$ and $\mathbf{p}_{34}$; for E_q we use $(q^2+m_N^2)^{1/2}$. The two-dimensional integral is over the component of $\mathbf{q}$ perpendicular to $\mathbf{p}_{34}$. The $\mp$ signs in (6) and (7) are required by the antisymmetrization. The amplitudes A_{LMS} in (6) and B^a_{LMS} in (7) are linear combinations of the NN amplitudes. The pn rescattering term and two FSI terms in (3) contribute amplitudes similar to (7). The single-nucleon deuteron wave function components $\Phi_M^M(\mathbf{q})$ are calculated from the Paris potential (Ref. 29). To calculate differential cross sections one substitutes the T matrix from (6) and (7) for all six diagrams into Eq. (5).

The usual form of the $(p,2p)$ cross section, as written in formula (1) in Sec. I, is the contribution of the first term IA_{pp} in the multiple-scattering expansion (3). Substituting (6) into (5) gives formula (1) as follows:

$$\begin{aligned}\frac{d^3\sigma}{d\Omega_3 d\Omega_4 dT_3}&=\frac{s_{34}p_3p_4^2}{p_1(E_5p_4-p_5E_4\cos\theta_{45})}\times\sum_{m,m'}|\langle m'|F^{pp}_{\text{c.m.}}(\theta,\phi)|m\rangle|^2|\Phi(\mathbf{p}_5)|^2\\&=K(d\sigma/d\Omega)^{pp}_{\text{c.m.}}|\Phi(\mathbf{p}_5)|^2\ .\end{aligned}\tag{8}$$

D. Results of the calculation

Only results of the multiple-scattering (MS) calculation relevant to the data presented in this part (I) will be

shown here. If one defines ratios of the calculated differential cross section, including the impulse approximation and one second-order graph at a time, to the IA_{pp} differential cross section

$$R_i = | T_{IA}^{pp} + T_{IA}^{pn} + (1/4\pi)T_i |^2 / | T_{IA}^{pp} |^2 , \quad (9)$$

and of the global result including all graphs, to the impulse approximation differential cross section

$$R_{\text{global}} = \left| T_{IA}^{pp} + T_{IA}^{pn} + (1/4\pi) \sum_{i=a}^{d} T_i \right|^2 / |T_{IA}^{pp}|^2 , \quad (10)$$

then $(R-1)$ is the percentage correction to be applied to the pp IA according to the calculation. Figure 6 shows these results for the 41.5°-41.4° kinematics as a function of p_5, the neutron recoil momentum. It should be noted that graphs (b), (c), and (d) in Fig. 5 give a negative correction to the cross section, and therefore to the ratio R, while (a) produces a positive one [not shown because $(R-1)$ is smaller than 10^{-3}]. The overall correction $(R_{\text{global}}-1)$ is negative, indicating that the full calculation gives a smaller result than IA_{pp}. The size of the correction ranges from 1% to 10%. The filled and empty symbols in this figure are a way to separate the two kinematical branches corresponding to the proton in the MRS magnetic spectrometer having a momentum larger than in the zero recoil configuration (for equal proton angles), from the one with the MRS proton having a smaller momentum than in the zero recoil situation. As these two kinematics are evidently symmetric, the differential cross sections ought to be the same, and so they are for each of the four contributions (a) through (d) as well as for the global differential cross section in Fig. 5. The only other check available was in reproducing the results of Wallace at 600 MeV, and there, again, the agreement was good. Additional results from this calculation can be found in Refs. 28 and 32.

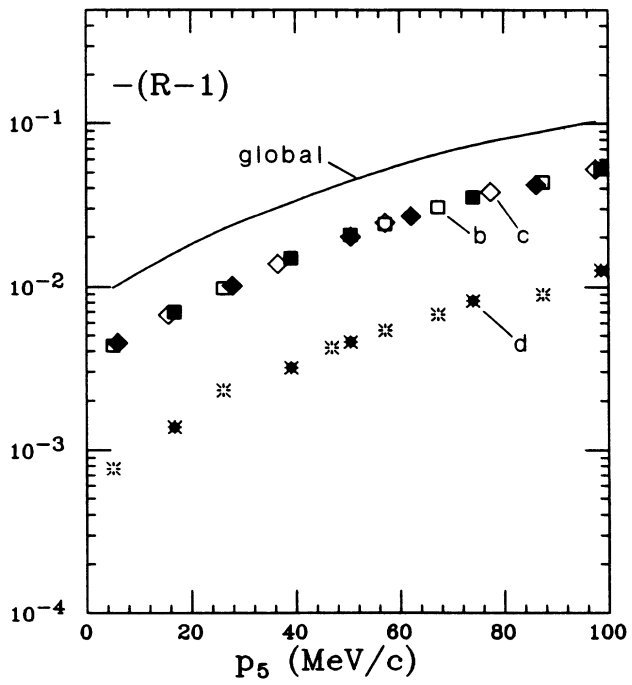

FIG. 6. The calculated quantity $-(R-1)$ including all six graphs of Fig. 5 for the 41.5°-41.4° proton angle pair. The separate contributions from graphs (b), (c), and (d) are shown; graph (a) gives a positive value for $(R-1) < 10^{-3}$ which is not shown.

V. RESULTS OF THE EXPERIMENT

A. Presentation and experimental uncertainties

In this part, fivefold differential cross sections $d^3\sigma/d\Omega_3 d\Omega_4 dT_3$ will be presented versus the kinetic energy T_3. The corresponding momentum space density distributions $|\Phi(\mathbf{p}_5)|^2$, calculated from the cross-section data, will be shown as a function of the neutron recoil momentum p_5 as calculated from the momenta $\mathbf{p}_3$ and $\mathbf{p}_4$. All $|\Phi(\mathbf{p}_5)|^2$ data points are plotted at a value of $|\mathbf{p}_5|$ corrected according to the results of the Monte Carlo simulation described in Sec. III D. The experimental results are compared with the prediction of the IA and with the complete calculation.

Preliminary results were presented in Ref. 33. A selection of data limited to equal angles and equal momenta for the two protons were published in Ref. 34. Small neutron recoil momentum data have been published in Ref. 28.

To facilitate the discussion of the data, the kinematics are grouped into three categories. In group one (Sec. V A 1) those kinematics are placed which include the neutron recoil momenta approximately equal to zero, and which are therefore called quasifree. Group two (Sec. V A 2) contains those kinematics which have pairs of equal proton angles, away from the quasifree region. Finally, group three contains (Sec. V A 3) kinematics situations with unequal proton angle pairs. These different kinematics, although all in the neutron momentum region 0 to 200 MeV/c, differ in the relative energy of the three NN pairs of the final state and in the direction of $\mathbf{p}_5$ relative to the beam direction. In Fig. 7 the kinematical relationship between $\mathbf{p}_5$ and $\mathbf{p}_3$ is shown for all kinematics discussed here, the labels corresponding to the three groups. The error bars in all following figures represent statistical uncertainties only, including the contribution generated by the removal of accidental events.

The systematic errors affect the results in two separate ways: the differential cross sections are uncertain because of systematic errors in monitor calibration, target thickness, solid angle, and energy interval definitions. In addition, when the data are analyzed in terms of the neutron recoil momentum, the systematic uncertainty in p_5 must be folded in; the latter comes from uncertainties in the angles θ_3 and θ_4 and energy T_3, and in the correction applied to take into account finite acceptances. As described in Sec. III B the elastic pp differential cross section has been measured with the same apparatus, at the same angles as the group 1 $(p,2p)$ data and the results were used to determine the target thickness. As a consequence the systematic uncertainties for the $(p,2p)$ data come mainly from $\Delta T_3 \Delta\Omega_4$ and from the target thick-

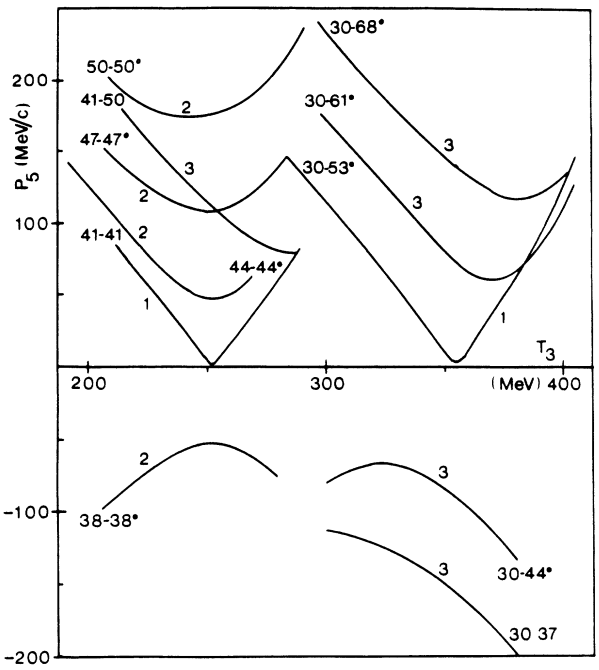

FIG. 7. Kinematical diagram showing the relation between neutron recoil momentum and kinetic energy of proton on the left-hand side. A negative sign for p_5 indicates a neutron momentum opposite to the incident proton momentum $\mathbf{p}_1$. Labels refer to subsections in Sec. V A.

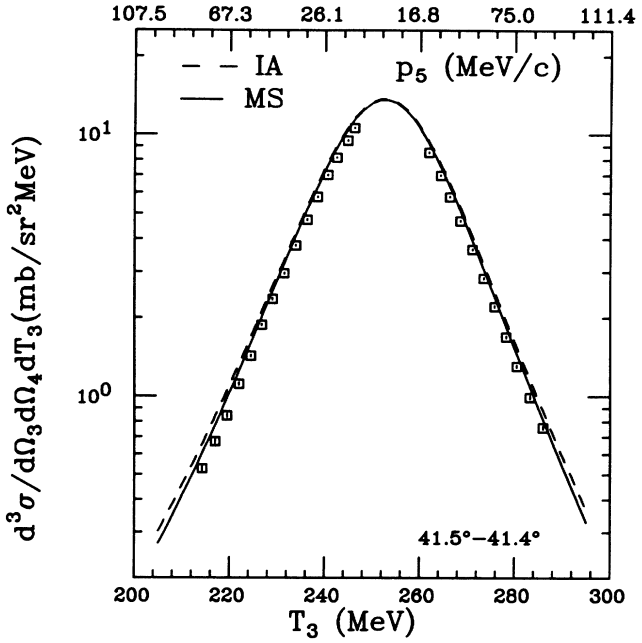

FIG. 8. The $(p,2p)$ differential cross section $d^3\sigma/d\Omega_3 d\Omega_4 dT_3$ for the proton angle pair 41.5°-41.4° as a function of the kinetic energy of the proton on the left-hand side, T_3.

ness: a combined value of ±1.8% is estimated for these contributions. In addition these data have an uncertainty in p_5 of ±0.9 MeV/c to ±0.6 MeV/c for $15<p_5<80$ MeV/c, which must be folded in when one calculates $|\Phi(\mathbf{p}_5)|^2$ and compares with a theoretical momentum distribution; in this case, although the target thickness does not enter, the total systematic uncertainty increases, because of the uncertainty in p_5, to ±2.2% near $p_5=80$ MeV/c, and to ±2.7% near 15 MeV/c.

1. *Quasifree kinematics*

Figure 8 shows the differential cross section for the 41.5°-41.4° angle pair. The abscissas give both the kinetic energy T_3 and the recoil momentum ($\mathbf{p}_5=-\mathbf{q}$) of the spectator neutron. The statistical errors are between 0.4 and 1.5%. As explained in Sec. V A, the total systematic uncertainty for the differential cross sections is ±1.8%. The data are compared with the IA prediction (dashed curve), calculated using the Paris potential deuteron wave function, and with the complete calculation (solid curve). All data points are below either one of or both of the two theoretical curves. To better display this systematic difference between data and theoretical predictions, the ratio $R=d^3\sigma(\text{data})/d^3\sigma(\text{IA}_{pp})$ is shown in Fig. 9 vs p_5 (MC). A similar figure has been shown previously in Ref. 28; however, following publication of those data an underestimate in the drift chamber efficiency was found, corresponding to a decrease in the values of R of 2.9%. The results of the complete calculation with the Paris deuteron wave function are shown as the dashed curve for the ratio $R=d^3\sigma(\text{MS})/d^3\sigma(\text{IA}_{pp})$; the dotted-dashed curve is the ratio obtained with the Moscow deuteron wave function of Ref. 30.

The data in Fig. 9 are compatible with a constant value of R over the range of p_5 shown, and the mean missing

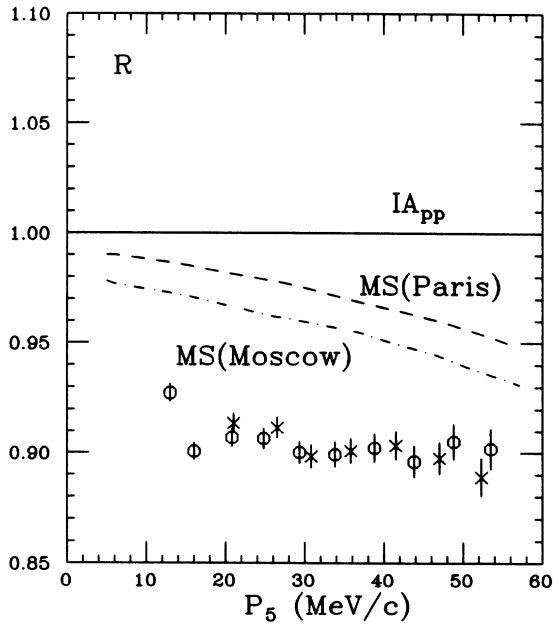

FIG. 9. Ratio R of the experimental differential cross section divided by the IA_{pp} prediction for the Paris wave function for small neutron momenta from the 41.5°–41.4° data. The symbols (○) and (×) have the same meaning as in Fig. 4. Dashed curve is R for complete calculation with the Paris wave function MS (Paris); dotted-dashed curve for complete calculation with Moscow wave function MS (Moscow).

strength is [9.41(±0.8)±2.5]%, where the error in parentheses is the standard deviation, and the second error is the systematic uncertainty; note that the uncertainty in R is independent of the uncertainty in the target thickness for these data. Compared with the complete calculation, the missing strength is reduced by 1% to 5% depending on p_5; however, the assumption of a constant value for R is not justified in this case. As in Ref. 28 one concludes that there exists an irreducible discrepancy between the data and the plane-wave impulse approximation (PWIA) prediction in the region of $p_5 < 60$ MeV/c which is in overall agreement with the results of previous experiments, although the total experimental uncertainty on the missing strength is now approximately four times smaller than was the case prior to this experiment. The irreducible discrepancy is also approximately four times the size of the systematic uncertainty of the data.

The differential cross-section data for the angle pair 30.1°-53.7° are show in Fig. 10; they appear closer to the theoretical prediction of the IA_{pp} and of the complete calculation than the data in Fig. 8. However, as discussed in Sec. III B, the value of the elastic pp differential cross section for 66° c.m. scattering angle found in the present experiment is 6% larger than the phase-shift value of Ref. 24. Using the measured value of the pp cross section would shift both theoretical curves upwards by approximately 6%; the data would then show approximately the same missing strength as in Fig. 9.

The momentum density $|\Phi(\mathbf{p}_5)|^2$ obtained using (1) in Sec. I. for the proton angle pair 30.1°-53.7° is compared with the 41.5°-41.4° data in Fig. 11. For $|\Phi(\mathbf{p}_5)|^2$ the systematic uncertainty is in the range 2.2 to 2.5% for $p_5 < 80$ MeV/c. Here the pp differential cross section used in (1) for the 30.1°-053.7° is the one obtained in the present experiment. A larger p_5 range is shown in this figure than in the previous one, and as a result the systematic uncertainties are not everywhere as small as discussed above. Yet it is obvious that the results from both kinematics are excellent agreement where they overlap, i.e., up to $p_5 = 80$ MeV/c.

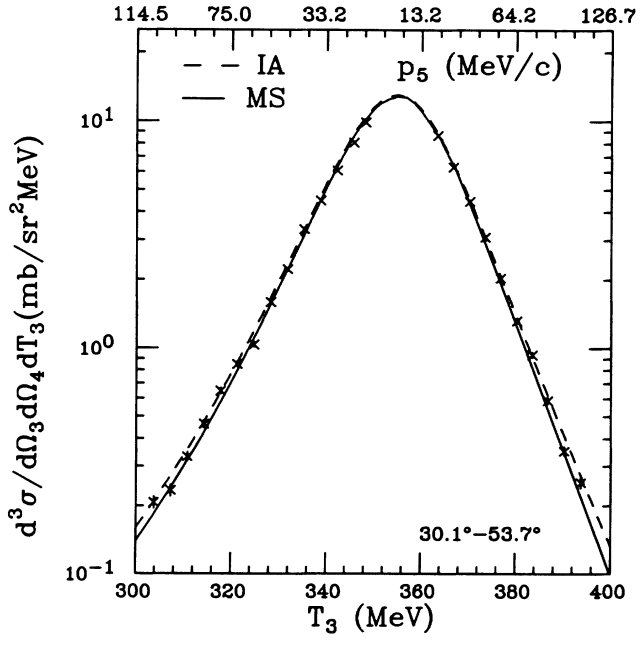

FIG. 10. Same as Fig. 8, but for 30.1°-53.7°.

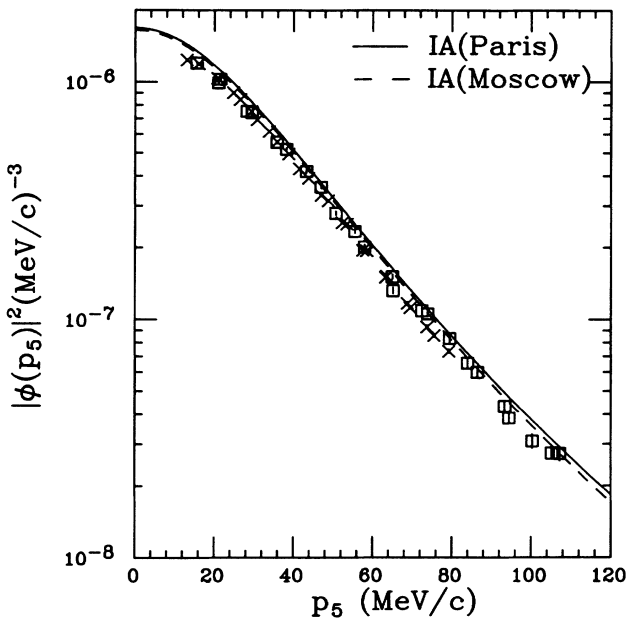

FIG. 11. Momentum density $|\Phi(\mathbf{p}_5)|^2$ obtained from formula (1), for the data of Figs. 8 (□) and 10 (×). The solid curve is for the Paris wave function and the dashed curve for the Moscow wave function, both in impulse approximation (IA).

2. *Equal proton angle pairs*

In Figs. 12(a) and 12(b) are shown the differential cross sections for symmetric angles 38.1°-38.0° and 44.1°-44.0°, respectively. The dashed curves are the PWIA predictions, and the solid curves are the results of the complete calculation with the Paris potential wave function. The data in Fig. 12(a) are lower than the IA prediction, while in Fig. 12(b) the data are in excess of the IA. In the first case the complete calculation goes in the right direction, but in the second case the discrepancy increases when comparing with the complete calculation. To further study this behavior, the same data are used to obtain the $|\Phi(\mathbf{p}_5)|^2$ values according to (1) and displayed in Fig. 13(a). The point should be made here that the momentum of the struck proton $\mathbf{q}$ is parallel to the projectile momentum for the 38.1°-38.0° data, i.e., $\mathbf{q}\cdot\mathbf{p}_1/|\mathbf{q}\cdot\mathbf{p}_1| > 0$, but antiparallel for 44.1°-44.0° ($\mathbf{q}\cdot\mathbf{p}_1/|\mathbf{q}\cdot\mathbf{p}_1| < 0$). Obviously different values of $|\Phi(\mathbf{p}_5)|^2$ are obtained for the two data sets. One interpretation of this result is that it reflects incorrect handling of the off-shell NN vertex for IA (see Sec. IV A). A number of schemes exist which propose different ways to resolve the off-shellness ambiguity. One of these schemes is based on the infinite momentum frame dynamics (Frankfurter and Strickman[35]), and assumes that both constituents of the deuteron are on-shell. The internal momentum k_F thus

defined is larger than p_5 for the data in Fig. 12(a), but smaller for the data in Fig. 12(b). Another scheme is based on the assumption that energy and momentum must be transferred to both constituents of the deuteron prior to the *NN* interaction (Gugelot[36]), and is in essence a binding and recoil energy correction. It leads to a redefinition of the internal momentum q_{BC} to the frame in which both nucleons have zero sum momentum, which is not the laboratory frame. Again, q_{BC} is different from p_5, very much in the same way as with k_F. The $|\Phi(\mathbf{p}_5)|^2$ values of Fig. 13(a) are shown again in Fig. 13(b), but this time versus k_F. The agreement between the two sets of results is much improved with k_F, and a similar result would be obtained with q_{BC}.

The data for the two other symmetric angle pairs, 47.1°-47.0° and 50.0°-50.0°, are shown in Figs. 14(a) and 14(b). The data points in Fig. 14(a) are in good agreement with the IA and the complete calculation. In Fig.

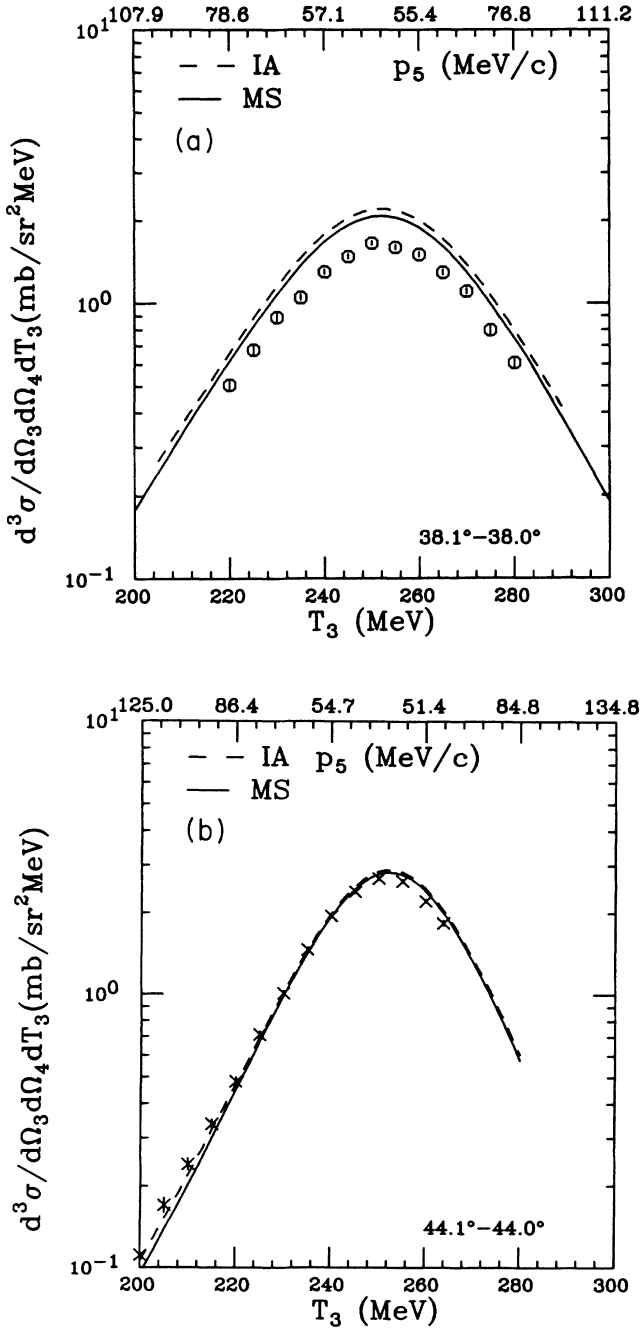

FIG. 12. Differential cross section vs lhs proton kinetic energy T_3 for the proton angle pairs 38.1°-38.0° in (a) and 44.1°-44.0° in (b).

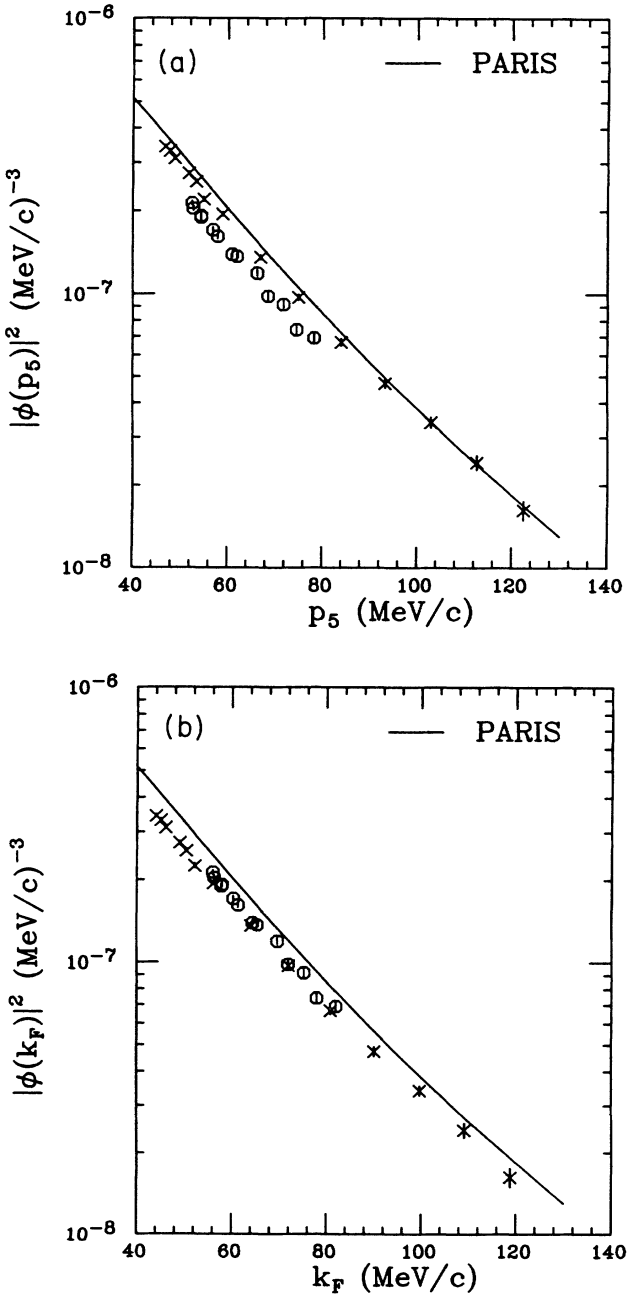

FIG. 13. Momentum density for the 38.1°—38.0° data (○) and 44.1°—44.0° data (×) vs p_5 in (a) and vs the internal momentum defined in the infinite momentum frame k_F in (b).

14(b) the data are much lower than the IA, and although the complete calculation does come closer to the data, it still fails to predict the measured differential cross section by up to 30%. The systematic uncertainty for the angle pairs 38.1°-38.0°, 44.1°-44.0°, and 47.1°-47.0° is ±5%, while it is ±8% for the 50.0°-50.0° data.

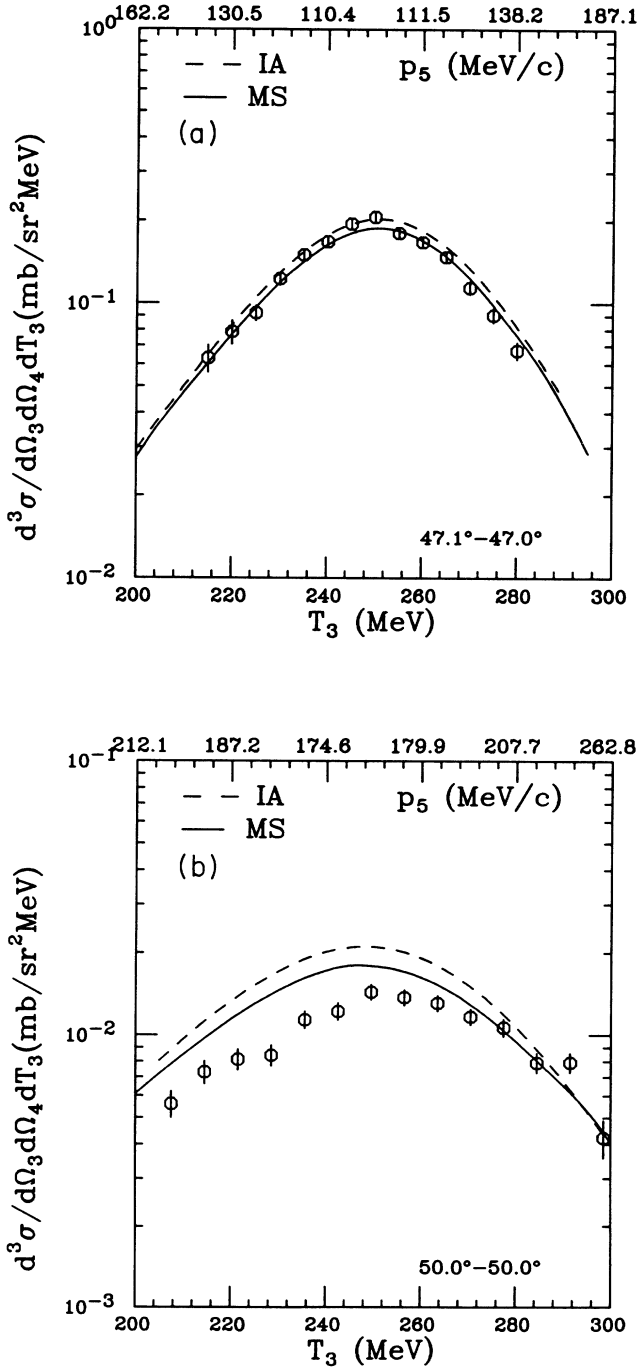

FIG. 14. Differential cross section vs lhs proton kinetic energy T_3 for the proton angle pairs 47.1°-47.0° in (a) and 50.0°-50.0° in (b).

3. *Unequal proton angles*

In order to explore the three-body phase space to the fullest extent possible, additional data were obtained at a number of unequal angle combinations away from quasi-free conditions. Most of these results will be presented in part II of this work, but here the small recoil data at the angle pairs 30.1° with 37.0°, 44.0°, 61.0°, and 68.0°, as well as the angle pair 41.5°-50.0° are shown.

The differential cross sections for these five angle pairs are presented in Figs. 15(a) to 15(e). Again the data are compared with the IA prediction (dashed curves) and the complete calculation (solid curves). The data in Figs. 15(a) and 15(b) are lower than the IA at small T_3, then cross over and are in excess at large T_3. The complete calculation is 5% to 10% lower than the IA; it decreases the discrepancy at low T_3 values but increases it at the higher T_3 values.

The data in Fig. 15(c) are in good agreement with the IA and the complete calculation at all T_3 values, while in Fig. 15(d) the data are in better agreement with the IA than with the complete calculation.

Finally, the data in Fig. 15(e) are somewhat higher than the IA up to T_3=240 MeV; the complete calculation reproduces the data better near q=80 MeV/c, but worse near q=180 MeV/c. The systematic uncertainty for all four angle pairs (EX84) is ±5%.

As with the 38.1°-38.0° and 44.1°-44.0° data in Sec. V A 2, the 30.1°-44.0° and 30.1°-61.0° data correspond to collisions with a proton momentum parallel and antiparallel to the projectile momentum, respectively. Again the first kinematics gives Φ^2 values near minimum p_5 which are smaller than the second. Use of either k_F or q_{BC} instead of p_5 would remove this discrepancy. However, in the large p_5 region the two data sets deviate from the IA in opposite ways, and this cannot be corrected with either k_F or q_{BC}.

VI. CONCLUSIONS

The detailed discussion in Sec. V indicates that overall the data are in fair agreement with the IA for all proton angle pairs. A better overview is seen Fig. 16 which shows the single-nucleon momentum space density $|\Phi(\mathbf{p}_5)|^2$ as a function of the neutron recoil p_5 for all data up to 200 MeV/c. Up to 150 MeV/c the data scatter is typically ±10%, with the mean value ≈10% below the Paris potential $|\Phi(\mathbf{p}_5)|^2$ distribution. In this kinematical range the results of the complete calculation never differ from the IA by more than 10%, typically 1–10%, and are systematically lower than the IA. One conclusion is that the missing strength observed in the limited range $15<p_5<60$ MeV/c (Ref. 34) does persist up to about 150 MeV/c. These results also confirm previously reported indications of a missing strength in the ^{2}H(p,2p)n reaction in a more detailed way and more precisely than available before.

Integrating $p_5^2|\Phi(\mathbf{p}_5)|^2$ from 0 to 150 MeV/c with the

Paris potential wave function, one finds the probability for a proton in this interval of internal momentum to be ≈ 0.85. Thus the mapping of the momentum space density distribution $|\Phi(\mathbf{p}_5)|^2$ obtained in this work covers most of the internal momentum phase space, and this establishes the observed missing strength of $\approx 10\%$ as a failure to observe more than 90% of one proton in the deuteron on the basis of the $(p,2p)$ reaction at 500 MeV.

The IA $|\Phi(\mathbf{p}_5)|^2$ values obtained from the $^2\mathrm{H}(e,e'p)n$ data of Ref. 12 are shown together with the 41.5°-41.4° and 41.5°-50.0° data from the present work and $^2\mathrm{H}(p,2p)n$ data of Ref. 11 in Fig. 17; there are also unpublished $^2\mathrm{H}(p,2p)n$ data at 1.0 GeV,[37] not shown in Fig. 17, which are in overall agreement with the present data in the $p_5 \leq 200$ MeV/c range. The electron data do indeed show a similar, even larger missing strength when compared with the Paris potential $|\Phi(\mathbf{p}_5)|^2$ distribution. However, Arenhoevel[14] has calculated corrections includ-

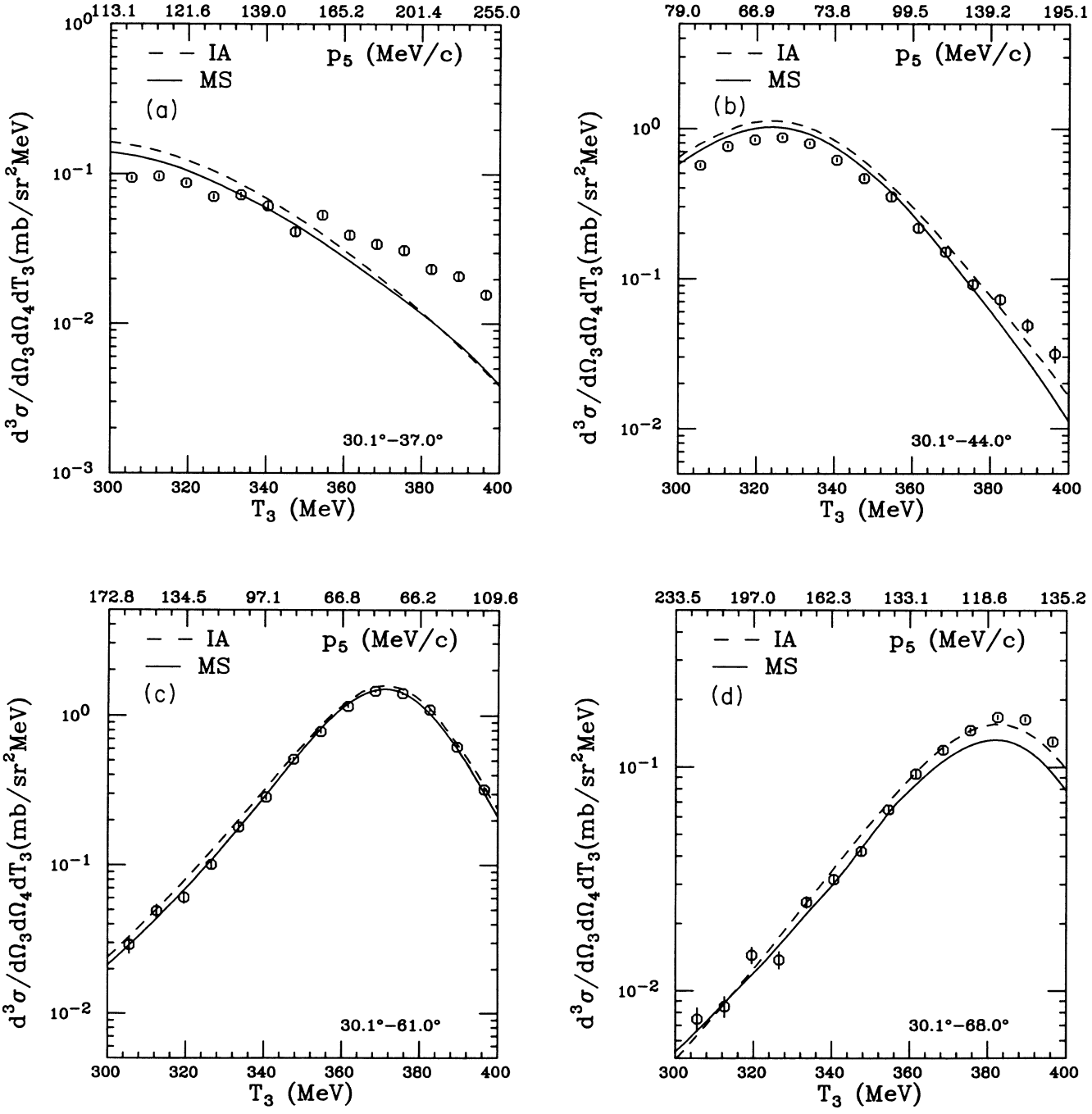

FIG. 15. Same as Fig. 14 but for the proton angle pairs 30.1° with 37.0° in (a), with 44.0° in (b), with 61.0° in (c), with 68.0° in (d), and 41.5° -50.0° in (e).

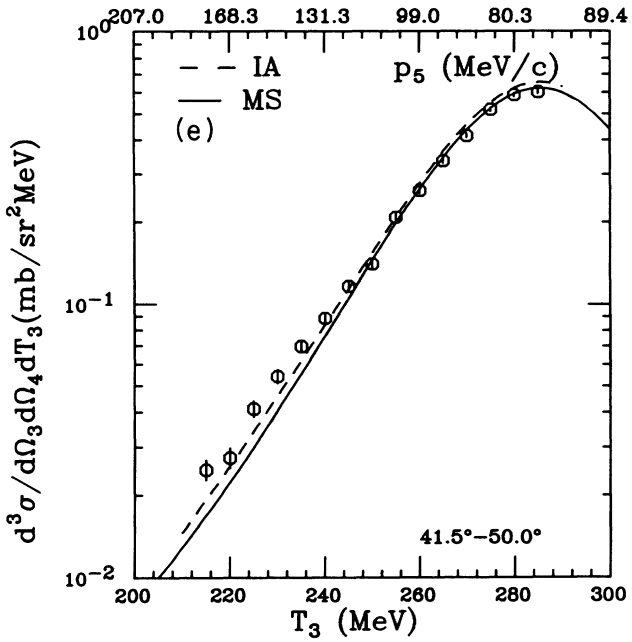

FIG. 15. (*Continued*).

ing MEC, IC, and FSI for the electron data and has shown that these corrections partially account for the discrepancy. No significant MEC correction is expected for the proton data; the complete calculation has shown that double scattering and FSI corrections are always small for these data. Finally, it appears unlikely that the discrepancy is due to the approximation made in using on-energy-shell *NN* amplitudes, because the struck nucleon is nearly on-shell, at least for the IA process. For the double scattering and FSI contributions much larger off-shellness is encountered, and significant errors could result from the approximation; however, the corrections generated by these graphs always remain in the few percent range for the neutron momenta included here. In conclusion, it appears that better calculations are required than the ones discussed here to explain the apparent proton missing strength established by the data. In particular the use of a covariant deuteron wave function and relativistic treatment of the scattering problem, together with a better treatment of the off-shell problem, might provide the explanation. The quality of the present data would now appear to warrant such theoretical investigations. Only after such studies have been done could one be in a position to consider more exotic effects, such as non-nucleonic components in the deuteron, to explain the missing strength.

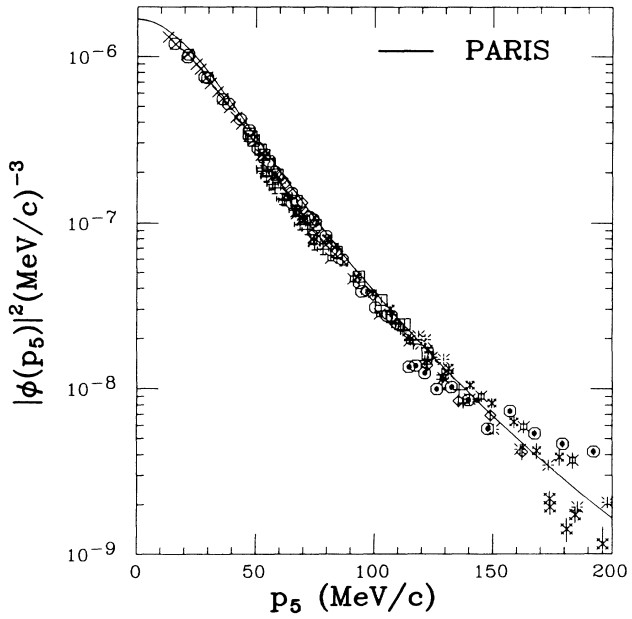

FIG. 16. All values of the momentum density $|\Phi(\mathbf{p}_5)|^2$ presented in this paper, shown vs the neutron momentum p_5: 41.5°-41.4°(×); 30.1°-53.7° (○); 38.1°-38.0° (✣); 44.1°-44.0° (□); 47.1°-47.0° (+); 50.0°-50.0° (✱); 30.1°-37.0° (◉); 30.1°-44.0° (⌑); 30.1°-61.0° (◇); 30.1°-68.0° (✳); and 41.5°-50.0° (✕).

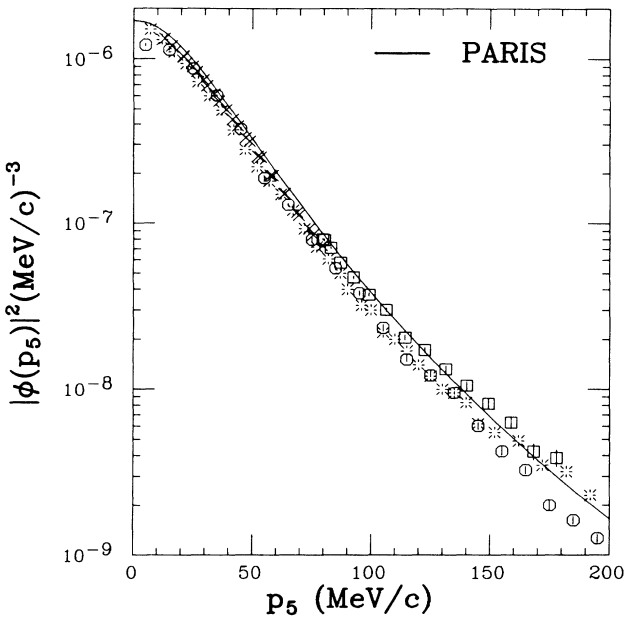

FIG. 17. Momentum density vs neutron momentum for the 41.5°-41.4° data (×), and the 41.5°-50.0° data (□) from this experiment, compared with the $(p,2p)$ results of Felder *et al.* (✳). Also included are the $(e,e'p)$ results of Bernheim *et al.* (○).

ACKNOWLEDGMENTS

The success of this experiment would not have been possible without the great dedication of the TRIUMF staff. Various people were involved at different stages of this project. Dr. D. A. Hutcheon, Dr. C. A. Miller, Dr. P. W. Green, and Dr. J. Tinsley helped at TRIUMF. Dr. Jon M. Wallace at Los Alamos Scientific Laboratory and Professor R. A. Arndt at Virginia Polytechnic Institute and State University provided help and encouragement during the calculation. This work was supported by Grant Nos. PHY82-03431, PHY83-04320, PHY85-09880, and PHY82-18386 from the National Science Foundation of the United States and by the Natural Sciences and Engineering Research Council of Canada. One of us (H.P.) is grateful for a North Atlantic Treaty Organization travel grant.

*Present address: Istituto di Fisica, Universita di Milano, I 20133, Milano, Italy.
†Mailing address: TRIUMF, Vancouver, British Columbia, Canada.
‡Present address: Pharma Department, Sandoz AG, CH4002 Basel, Switzerland.
§Present address: Jet Propulsion Laboratory, Pasadena, CA 91109.
**Present address: University of Victoria, Victoria, British Columbia, Canada V8W 2Y2.
††Present address: Koningligke Marine, den Helder, The Netherlands.

[1]R. Serber, Phys. Rev. **72**, 1008 (1947).
[2]G. F. Chew and G. C. Wick, Phys. Rev. **85**, 636 (1952).
[3]G. Jacob and Th. A. J. Maris, Rev. Mod. Phys. **38**, 121 (1966).
[4]M. Riou, Rev. Mod. Phys. **37**, 375 (1965).
[5]D. F. Jackson and T. Berggren, Nucl. Phys. **62**, 353 (1965).
[6]P. Kitching, W. J. McDonald, Th. A. J. Maris, and C. A. Z. Vasconceiios, in *Advances in Nuclear Physics,* edited by J. W. Negele and E. Vogt (Plenum, New York, 1985), Vol. 15, p. 43.
[7]F. Gross, Phys. Rev. **186**, 1448 (1969).
[8]R. Blanckenbecler and R. Sugar, Phys. Rev. **142**, 1051 (1966).
[9]C. F. Perdrisat, L. W. Swenson, P. C. Gugelot, E. T. Boschitz, W. K. Roberts, J. S. Vincent, and J. R. Priest, Phys. Rev. **187**, 1201 (1969).
[10]T. R. Witten, M. Furic, G. S. Mutchler, C. R. Fletcher, N. D. Gabitzsch, G. C. Phillips, J. Hudomalj, L. Y. Lee, B. W. Mayes, J. C. Allred, and C. Goodman, Nucl. Phys. **A254**, 269 (1975).
[11]R. D. Felder, T. R. Witten, T. M. Williams, M. Furic, G. S. Mutchler, N. D. Gabitzsch, J. Hudomalj-Gabitzsch, J. M. Clement, G. C. Phillips, E. V. Hungerford, L. Y. Lee, M. Warneke, B. W. Mayes, and J. C. Allred, Nucl. Phys. **A264**, 397 (1976).
[12]M. Bernheim, A. Bussiere, J. Mougey, D. Royer, D. Tarnowski, S. Turck-Chieze, S. Frullani, G. P. Capitani, E. de Sanctis, and J. Jans, Nucl. Phys. **A365**, 349 (1981); S. Turck-Chieze, P. Barreau, M. Bernheim, P. Bradu, Z. E. Meziani, J. Morgenstern, A. Bussiere, G. P. Capitani, E. de Sanctis, S. Frullani, F. Garibaldi, and J. Mougey, Phys. Lett. **142B**, 145 (1984).
[13]H. Breuker, V. Burkert, E. Ehses, U. Hartfiel, G. Knop, G. Kroesen, J. Langen, M. Leenen, W. Mehnert, A. Samel, R. Sauerwein, H. D. Schablitzky, and G. Schnicke, Nucl. Phys. **A455**, 641 (1986).
[14]H. Arenhoevel, Nucl. Phys. **A384**, 287 (1982).
[15]R. Vinh Mau, in *Mesons in Nuclei,* edited by M. Rho and D. Wilkinson (North-Holland, Amsterdam, 1979), Vol. I, p. 151.
[16]R. V. Reid, Ann. Phys. (N.Y.) **50**, 211 (1968).
[17]H. J. Sebel, Technische Hogeschool Delft Report No. 84-5, 1984.
[18]C. A. Goulding and J. G. Rogers, Nucl. Instrum. Methods **153**, 511 (1978).
[19]A. W. Stetz (unpublished).
[20]W. Bertozzi, M. V. Hynes, C. P. Sargent, W. Turchinetz, and C. Williamson, Nucl. Instrum. Methods **162**, 211 (1979).
[21]A. Bracco, H. P. Gubler, D. K. Hasell, W. T. H. van Oers, R. Abegg, C. A. Miller, M. B. Epstein, D. A. Krause, D. J. Margaziotis, and A. W. Stetz, Nucl. Instrum. Methods **219**, 329 (1984).
[22]P. Chatelain, B. Favier, F. Faroughi, J. Hoftiezer, S. Jaccard, J. Piffaretti, P. Walden, and C. Weddingen, J. Phys. G **8**, 643 (1982).
[23]D. Ottewell, P. Walden, E. G. Auld, G. Giles, G. J. Lolos, B. J. McParland, and W. R. Walk, Nucl. Phys. **A412**, 189 (1984).
[24]R. A. Arndt, L. D. Roper, R. A. Bryan, R. B. Clark, B. J. VerWest, and P. Signell, Phys. Rev. D **28**, 97 (1983). Phase shift from SAID, solution SP88 0–1.3 GeV.
[25]G. W. Hoffmann, M. L. Barlett, R. W. Fergerson, J. A. Marshall, J. A. McGill, E. C. Milner, L. Ray, and J. F. Amann, Phys. Rev. C **37**, 397 (1988).
[26]R. G. Glauber, in *Lectures in Theoretical Physics,* edited by W. E. Brittin and L. G. Dunham (Interscience, New York, 1959), Vol. I, p. 315.
[27]J. M. Wallace, Phys. Rev. C **5**, 609 (1972).
[28]V. Punjabi, C. F. Perdrisat, W. T. H. van Oers, P. R. Poffenberger, W. P. Lee, C. A. Davis, A. Bracco, D. J. Margaziotis, J. P. Huber, M. B. Epstein, H. Postma, H. J. Sebel, and A. W. Stetz, Phys. Lett. B **179**, 207 (1986).
[29]M. Lacombe, B. Loiseau, R. Vinh Mau, J. Cote, P. Pires, and R. de Tourreil, Phys. Lett. **101B**, 139 (1981).
[30]V. M. Krasnopol'sky, V. I. Kukulin, V. N. Pomerantsev, and P. B. Sazonov, Phys. Lett. **165B**, 7 (1985).
[31]H. P. Stapp, T. Ypsilantis, and N. Metropolis, Phys. Rev. **105**, 302 (1957).
[32]V. Punjabi, Ph.D. thesis, College of William and Mary, 1986.
[33]V. Punjabi *et al.,* Bull. Am. Phys. Soc. **29**, 647 (1984); **30**, 795 (1985); **30**, 1247 (1985); M. B. Epstein, Contribution C4 to the Tenth International Conference on Particles and Nuclei, Heidelberg, Federal Republic of Germany, 1984, edited by F. Güttner, B. Povh, and G. zu Putlit.
[34]C. F. Perdrisat, V. Punjabi, M. B. Epstein, D. J. Margaziotis, A. Bracco, H. P. Gubler, W. P. Lee, P. R. Poffenberger, W. T. H. van Oers, H. Postma, H. J. Sebel, and A. W. Stetz, Phys. Lett. **156B**, 38 (1985).
[35]L. L. Frankfurt and M.I. Strickman, Nucl. Phys. **B148**, 107 (1979).
[36]P. C. Gugelot, Phys. Rev. C **30**, 654 (1984).
[37]N. P. Aleshin, S. L. Belostotsky, Yu. V. Dotsenko, J. Ero, O. G. Grebenyuk, J. Kechkemeti, L. M. Kochenda, Zh. Kovach, L. G. Kudin, N. P. Kuropatkin, S. I. Manayenkov, O. V. Mikluho, V. N. Nikulin, O. E. Prokofjev, A. Yu. Tsaregorodtsev, and S. S. Volkov, Academy of Sciences USSR, Gatchina, Report No. 1259, 1987.

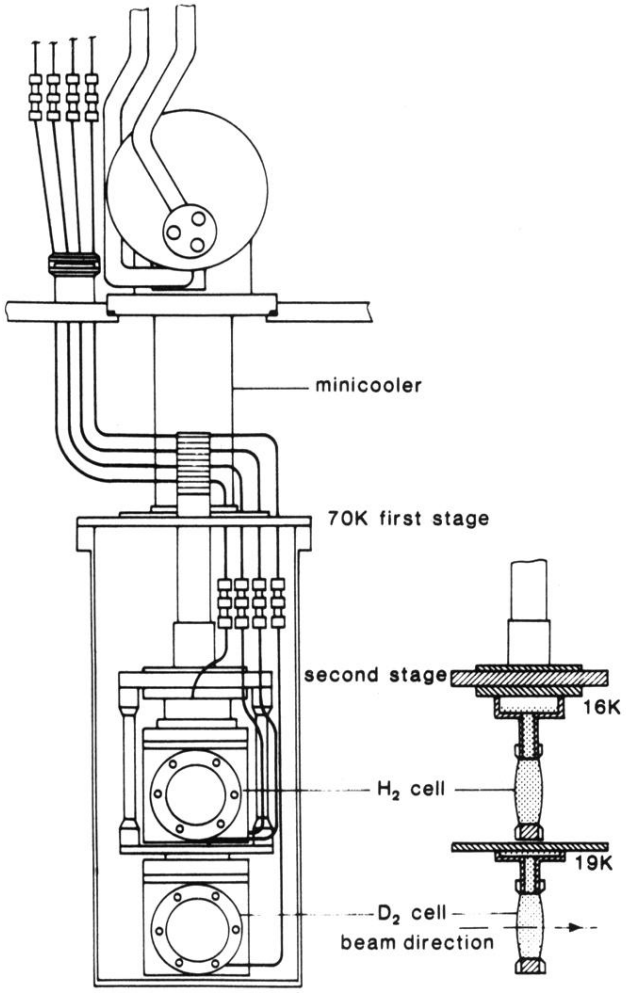

FIG. 2. Liquid hydrogen and deuterium cryostat, showing the geometry of the two target cells.